Ray-acoustic caustic formation and timing effects from ocean sound-speed relative curvature

Timothy F. Duda and James B. Bowlin
Applied Ocean Physics and Engineering Department, Woods Hole Oceanographic Institution, Woods Hole, Massachusetts 02543

(Received 12 November 1993; accepted for publication 3 March 1994)

Using deterministic ray-acoustic modeling of 1000-km propagation in the North Pacific, a depth-dependent parameter of ocean sound channels has been found to strongly influence geometrical ray propagation. This parameter is the sound speed times the second vertical derivative of sound speed divided by the square of the first derivative. Ray and wavefront timing and intensity can be influenced within realistic ocean sound channels by unpredictable wavefront triplications and caustics. These triplications are associated with large values of the parameter at ray turning points. The parameter, a relative curvature, behaves as a random variable because of ocean finestructure, causing the unpredictability. The relative curvature has a higher mean value near the sound-speed minimum for both an internal-wave model and actual data, so that this mechanism is a plausible explanation of poor multipath resolution and identifiability late in North Pacific pulse trains.

PACS numbers: 43.30.Cq, 43.30.Ft, 43.30.Pc

INTRODUCTION

In both the Slice89 experiment (Duda *et al.*, 1992) and the North Pacific gyre experiment (Dushaw *et al.*, 1993), multipath arrivals of pulses with 250 Hz center frequency have been resolvable early in the pulse train, but not late (Fig. 1). Multipath spacing is predicted to decrease towards the end of the pulse train, but ray-based predictions of fluctuations that obscure the multipath (Flatté and Stoughton, 1988) suggest that the identifiability transition should be later than is observed. The temporal smearing of the late, axially trapped energy is apparently more strongly dependent on structure peculiar to the sound-speed minimum than are the predicted fluctuations.

Calculations of ray paths depend strongly on the depth derivative of the sound speed. $\partial_z c$. Phase fluctuation calculations depend on the ray paths and ocean structure parameters (Flatté, 1983; Flatté and Stoughton, 1986; Flatté and Stoughton, 1988). Intensity fluctuation predictions depend on the statistics of relative ray positions, influenced by the second derivative of sound speed with respect to depth (Flatté, 1983; Flatté *et al.*, 1987). Neither of these contributors to arrival identifiability prediction has a sufficient link with the sound-speed minimum to explain the observations. We suggest but do not prove that the dimensionless parameter $U = c\ \partial_{zz}c/(\partial_z c)^2$, which grows large at the channel axis (it is actually unbounded), influences the identifiability. This parameter is referred to as the relative curvature. There is evidence that U is closely linked to nonlinear arrival-time fluctuations (those fluctuations associated with changing ray geometry) and offer this ray study as a simple diagnostic model of acoustic fluctuation in a spirit suggested earlier (Munk and Zachariasen, 1976a).

Predictability is important for acoustic remote sensing. A key part of a multipath propagation-based ocean acoustic remote sensing or detection systems is forward modeling of multipath. Given a model ocean sound-speed field and bathymetry, a forward model must predict when sound emitted from a source will arrive at a receiver and where the sound will travel. Three common forward models are normal modes, the parabolic equation, and geometric ray tracing (Boden *et al.*, 1991). Ray tracing is the most visually intuitive method to predict and study propagation, but it incorporates approximations that can give incorrect results, as do the others. Fully describing details of geometrical ray patterns formed within the wide range of true ocean waveguides (sound-speed profiles) and fully understanding the limits of the ray approach would be overwhelming tasks. We instead study ray patterns associated with a small set of closely related ocean waveguides, showing how high U at ray turning points leads to ray crossing and focusing. Real-ocean predictability is addressed by evaluating the depth distribution of U for a stochastic field of internal waves.

Consider an impulse of acoustic energy traveling along geometric rays radiating from a point source. The positions of energy along these rays at an instant in time, or positions of constant phase, define a wavefront. The wavefront is evident in either a range-depth diagram of energy at a fixed time or an arrival time-depth diagram at fixed range. The wavefront image at fixed time will be referred to as a rangefront, and the image at fixed range will be referred to as a timefront. These patterns have been considered since the early stages of acoustic tomography (Brown *et al.*, 1980; Munk and Wunsch, 1979). Timefront diagrams are analyzed here because the temporal snapshot rangefronts are not typically measured. General discussions of the physical processes will use the generic term wavefront.

In this study, timefronts calculated for closely related ocean sound-speed profiles are used to investigate sensitivity to U. Timefront structure is quantified by arrival time (phase), intensity, and caustic formation. High curvature of sound speed, which can either be included in or excluded from waveguide models that fit available data, produces small scale wavefront features. Similar features appear in

 0001-4966/94/96(2)/1033/14/$6.00

experimental results but are stochastic and transitory. Parabolic-equation simulation of the Slice89 propagation with internal-wave induced sound-speed structure shows very similar features (Colosi *et al.*, 1994). These features are not well-enough understood to be useful if one wishes to infer ocean structure using averages obtained from many transmissions or many nearby receivers, so minimization of these curvature effects is sensible for forward modeling of mean acoustic propagation. However, the high-curvature effects may be useful for studying ocean finestructure, and they offer an explanation for the lack of identifiability.

The separation of acoustic wavefronts into mean and fluctuating portions has difficulties comparable to those that arise with attempts to separate continua of scales in geophysical systems into distinct domains. Disciplines with such difficulties are turbulent diffusion (Henyey, 1989) and propagation of ocean internal waves (Müller *et al.*, 1986). Flatté (1983) has alluded to this difficulty in ocean ray acoustics. Aspects of the mean propagation may depend on the unpredictable small-scale structures, not just the large-scale structures. Our results suggest that wavefront overlapping, intensity fluctuation, and phase fluctuation which are neither predictable nor easily measured can occur from small-scale curvature structures, and these cannot be considered as zero-mean perturbations. These effects can be unpredictable for long-range ocean paths using contemporary knowledge of the ocean because of the non-uniqueness of sound-speed profiles which will fit available data. This nonpredictability would exist in either a fixed environment with unspecified curvature, as a result of poor sampling in depth, or an environment filled with stochastic finescale variability.

Elimination of spurious simulation effects is an important aspect of this work. The numerical ray calculation techniques are adequate and contribute negligible error. Details of the waveguide specification can lead to more substantial simulation errors, and an effort has been made to alleviate these. In particular, we have a simple technique to eliminate spurious non–turning point caustics, which are erroneous effects of physically unrealizable discontinuous second derivatives of sound speed. The effect is described in Sec. I, and the technique in Sec. II A.

Non–turning point caustics, which we feature throughout the paper, are discussed in Sec. I. Section II uses simulations to show the link between U and wavefront fluctuations for 1000-km propagation. The link is revealed through comparison of simulations using slightly varying ocean environments. Section III compares predicted and measured stochastic U statistics throughout the water column. Section IV is a summary.

I. NON–TURNING POINT CAUSTICS

Folds and caustics in wavefronts are linked to the dependence of horizontal (projected) ray velocity on initial ray angle ψ. In the simple case of a range-independent medium, define the change in group velocity versus ψ as

$$S_1 \equiv \frac{dv_1}{d\psi} \tag{1a}$$

$$= T^{-1}\left(\frac{dR}{d\psi} - v_1 \frac{dT}{d\psi}\right), \tag{1b}$$

where v_1 is the "group velocity" of a ray, defined as the quotient of horizontal range R and travel time T for one vertical ray oscillation [a double loop, using established terminology (Munk, 1974)]. The effect of sound-speed curvature on S_1 can be examined by expressing both $R(\psi)$ and $T(\psi)$ as integrals along the ray path.

To avoid repetition consider a general function F that can be written as

$$F(\psi) = 2\int_{z_l}^{z_u} f\, dz, \tag{2}$$

where $f = \partial F/\partial z$ and the limits z_u and z_l are the upper and lower turning points of the ray. To calculate the derivative of F with respect to ψ, first change to a derivative with respect to the sound speed at a turning point c_t,

$$\frac{dF}{d\psi} = \frac{dF}{dc_t}\frac{dc_t}{d\psi} \tag{3a}$$

$$= c_t \tan\psi \frac{dF}{dc_t}, \tag{3b}$$

where $\cos\psi = c_s/c_t$ has been used. Assuming that $c(z)$ is continuous, one may expand

$$\frac{dF}{dc_t} = 2\int_{z_l}^{z_u} \frac{\partial f}{\partial c_t}\, dz + \left(\frac{\partial z_u}{\partial c_t} f(z_u) - \frac{\partial z_l}{\partial c_t} f(z_l)\right), \tag{4}$$

and, since z_l and z_u are turning points themselves, this can be written

$$\frac{dF}{dc_t} = 2\int_{z_l}^{z_u} \frac{\partial f}{\partial c_t}\, dz + \frac{\partial z}{\partial c} f\Big|_{z_l}^{z_u}. \tag{5}$$

The second term on the right-hand side can be turned back into an integral by considering the derivative

$$\frac{d}{dz}\left(\frac{\partial z}{\partial c} f\right) = \frac{\partial f}{\partial c} - \frac{\partial^2 c/\partial z^2}{(\partial c/\partial z)^2} f, \tag{6}$$

so that

$$\frac{dF}{dc_t} = 2\int_{z_l}^{z_u}\left(\frac{\partial f}{\partial c_t} + \frac{\partial f}{\partial c} - \frac{\partial^2 c/\partial z^2}{(\partial c/\partial z)^2} f\right) dz. \tag{7}$$

The derivative of F can be put in the form

$$\frac{dF}{d\psi} = 2c_t \tan\psi \int_{z_l}^{z_u}\left(\alpha + \frac{c\,\partial^2 c/\partial z^2}{(\partial c/\partial z)^2}\beta\right)\frac{\partial s}{\partial z}\, dz, \tag{8}$$

with

$$\alpha \equiv \left(\frac{\partial}{\partial c_t} + \frac{\partial}{\partial c} + c_t^{-1} - (c_t + c)^{-1}\right)\frac{\partial F}{\partial s}, \tag{9a}$$

$$\beta \equiv \frac{1}{c}\frac{\partial F}{\partial s}, \tag{9b}$$

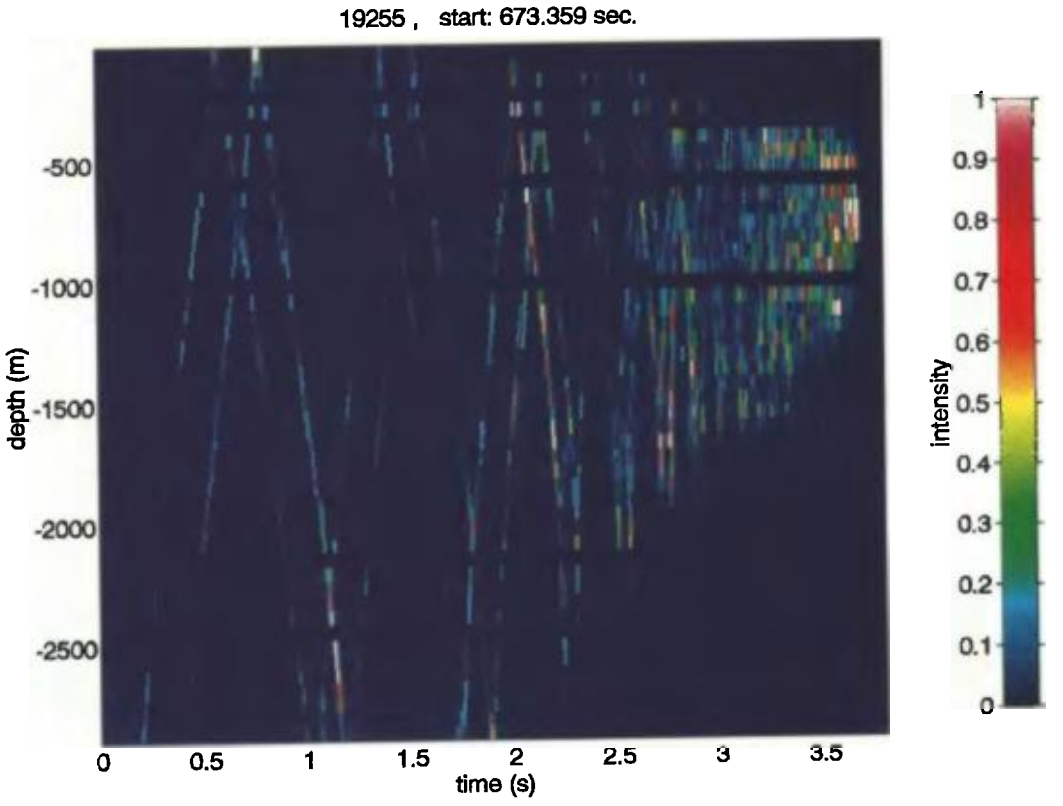

FIG. 1. Arrival time versus depth plot of intensity for one Slice89 arrival (Duda *et al.*, 1992) shows distinct timefronts (lines of high intensity in these coordinates) in only the early part of the pulse. The early energy has left the source at high angle and oscillates vertically in the sound channel. The timefronts after 2.8 s, which propagate in a region restricted near the c minimum, are not separable and identifiable. This distinct change is not in complete agreement with timing fluctuation and pulse-width predictions for the North Pacific. The intensity scale is arbitrary, with some clipping of high intensity. The travel time at time zero on the scale is given at the top, and the propagation distance is 1001 km.

and s denotes path length along the ray. There are two contributions to $dF/d\psi$. The term α will in general vary smoothly with ψ, while the β contribution can jump rapidly whenever both $c\ \partial_{zz}c/(\partial_z c)^2$ and $\partial s/\partial z$ are large, i.e., whenever there is a large curvature in the sound-speed profile near a turning point of a ray. For the particular cases of $F=T$ and $F=R$, the α and β terms can be found using $\partial T/\partial s=c^{-1}$ and $\partial R/\partial s=c/c_t$:

$$\alpha_T=c^{-1}c_t^{-1}-c^2-c^{-1}(c_t+c)^{-1}, \tag{10a}$$

$$\beta_T=c^{-2}, \tag{10b}$$

$$\alpha_R=c_t^{-1}-cc_t^{-1}(c_t+c)^{-1}, \tag{10c}$$

$$\beta_R=c_t^{-1}. \tag{10d}$$

Note that the α's and β's are bounded, smoothly varying functions.

In a weakly range-varying environment, we assume that the variable S has a dependence similar to that of S_1, with S defined using the horizontal ray velocity over a specific range rather than over a double loop. The travel-time rate of change $|S_1|$ can grow very large through the action of the β term. The factor $U=c\ \partial_{zz}c/(\partial_z c)^2$ can grow very large, with the limiting case of a singularity at a junction in a piecewise-linear (PWL) sound speed profile. It is finite for twice-differentiable profiles if $\partial_z c$ is not zero. The second factor $\partial s/\partial z=(\sin\theta)^{-1}$ has an integrable infinity (with respect to dz) at the turning points of the rays. The integral is unstable if U becomes too large at the turning point, enabling sudden jumps to large $|S_1|$. Any sign change in S_1, which may occur as S_1 moves to an extreme value, implies a zero crossing, corresponding to an extremum of v_1 and a wavefront reversal. A pair of wavefront reversals forms a wavefront triplication. Large U values can occur in any sound-speed profile, giving reversals, but they occur erroneously at junctions in PWL representations.

The importance of $\partial_{zz}c$ on eigentube structure and on intensity fluctuations within eigentubes has been pointed out in a series of articles by Flatté, Dashen, and collaborators (Dashen *et al.*, 1985; Flatté, 1983; Flatté *et al.*, 1987). They considered the structure within eigentubes associated with equilibrium rays defined by c and $\partial_z c$. Here, the unified effect of both the first and second derivatives on the equilibrium rays (the rays that define the wavefront) is explicitly examined using the parameter U.

Caustics appear in a wavefront at extrema of the function of depth at the receiver range versus launch angle, that is, where $dz_r/d\psi=0$. These points are coincident with $S=0$, the reversal criterion of a continuous wavefront. At these extrema, the finite amount of energy radiated over the launch angle interval $d\psi$ is concentrated over infinitesimal depth. This condition is often satisfied at portions of the wavefront near ray turning points, producing what we refer to as turn-

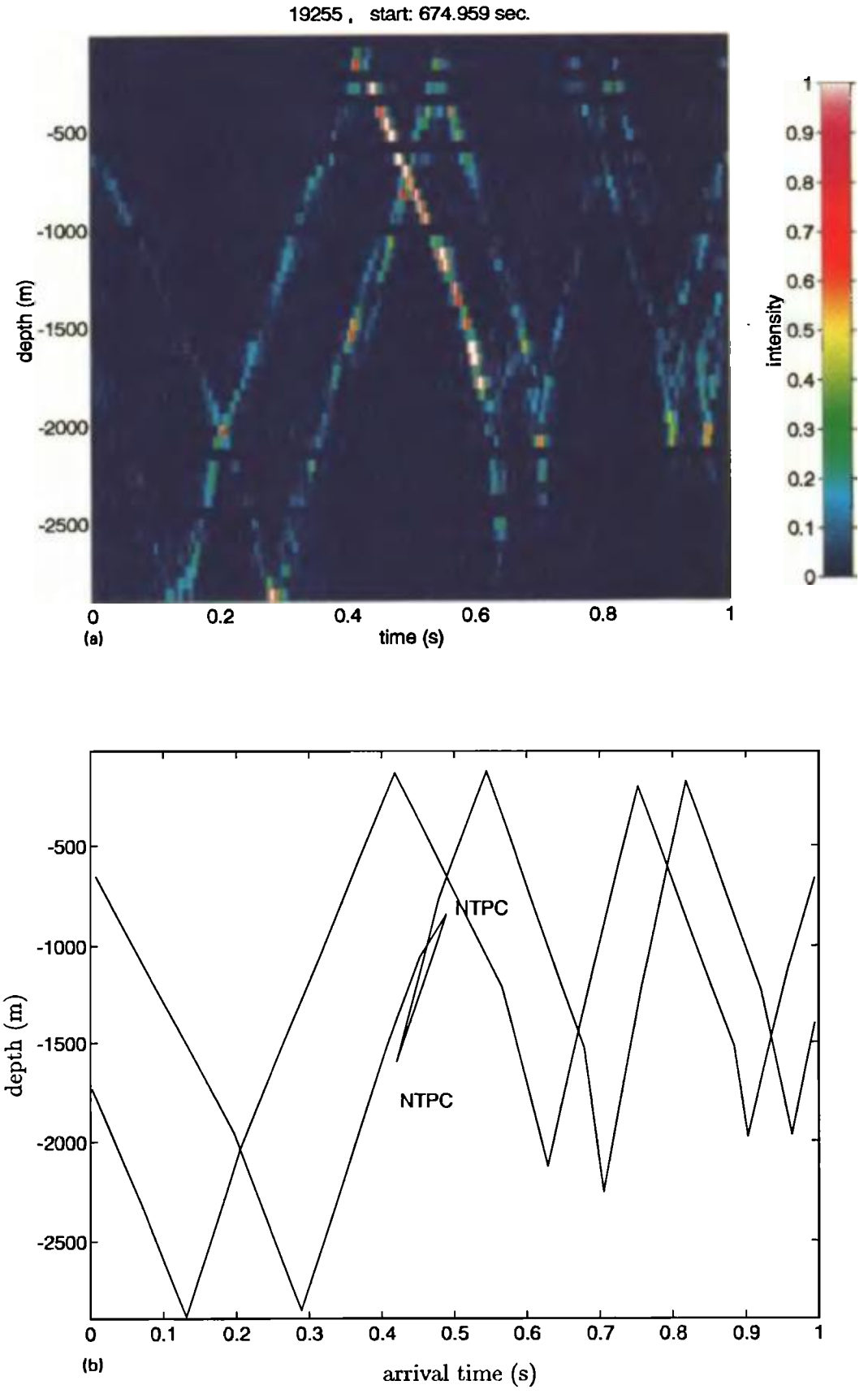

FIG. 2. (a) This expansion of the Slice89 timefronts of Fig. 1 shows NTP caustics and timefront folding. A clear timefront split or triplication, consistent with paired NTP caustics, can be seen in the left center of the frame. The travel time at time zero on the scale is listed above the frame. (b) The two bright features, marked with "NTPC," and the folded timefront are schematically shown.

ing point caustics. A caustic can also arise wherever there is a wavefront reversal resulting from a very large value of S_1 or S. These caustics are not necessarily associated with turning points, and are called non–turning point (NTP) caustics. A discrete layered derivation and calculation of the spurious NTP caustic effect of PWL profiles was made over 30 years ago (Pederson, 1961).

Nonspurious NTP caustics can occur for twice-differentiable sound-speed profiles. Section IV shows that the quantity and spatial separation of nonspurious NTP caustics, deduced from ray tracing, are systematically coupled with U. Experimentally, only two NTP caustics associated with triplication (Fig. 2) were clearly observed in the slowest 12 stable timefront segments analyzed for each of 283 transmissions (Duda *et al.*, 1992). The once-in-3400 occurrence of NTP caustics and triplication in the stable portion of the pulse is apparently caused by transient finestructure. The observed timefront turns close to the surface and may have encountered a feature at the base of the mixed layer. Intermittent regions of high intensity appearing along the timefront may be a related phenomena, caused by temporally unresolved triplication, giving merely caustics and localized intensity changes in full-wave propagation.

II. SIMULATION OF CURVATURE EFFECTS

The sensitivity of caustics and triplications to U is evaluated by ray tracing through related sound-channel environments with slight variations in curvature, thus variations in U. The family of environments is intended to model the Slice89 region.

A. Ray equation integration

The equations of motion governing rays can be written in Cartesian coordinates:

$$\frac{d\theta}{dr} = -c^{-1}\frac{\partial c}{\partial z} + c^{-1}\frac{\partial c}{\partial r}\tan\theta, \tag{11a}$$

$$\frac{dz}{dr} = \tan\theta, \tag{11b}$$

$$\frac{dt}{dr} = \frac{\sec\theta}{c}, \tag{11c}$$

where θ is the angle of the ray with respect to the horizontal r axis, and z is the vertical coordinate, positive upward. The first two are canonical equations that describe the ray trajectory. The third, which follows directly, gives travel time and is optionally included. The first equation is one component from the general expression for ray trajectory, derivable from Fermat's principle of least time (Bowlin *et al.*, 1993), and the other two are geometrical relations. The general expression for a trajectory (locus of $\mathbf{R}$), a generalized form of Snell's law of refraction, is

$$\ddot{\mathbf{R}} = \frac{\nabla n \perp \dot{\mathbf{R}}}{n} = n^{-1}[\nabla n - \dot{\mathbf{R}}(\nabla n \cdot \dot{\mathbf{R}})], \tag{12}$$

where $n = 1/c$ is the refractive index and the dot represents differentiation along the trajectory. It is seen that the component of refractive index gradient that is perpendicular to the trajectory is responsible for the change in direction, $\ddot{\mathbf{R}}$. The trajectory curvature vector $\ddot{\mathbf{R}}$ is always perpendicular to the unit vector tangent to the trajectory, $\dot{\mathbf{R}}$. We integrate the system using the fourth-order Runge–Kutta technique. The numerical integration contributes negligible error compared with effects due to variability of $c(r,z)$.

B. Sound-speed parametrization

Sound speed is required at arbitrary locations for accurate integration of the canonical equations. Analytic descriptions of $c(r,z)$ provide this, and can also have continuous slope to eliminate the NTP caustic effect. However, a twice differentiable parametrization of c allows systematic investigation of acoustic signatures from a wider class of ocean structures. Efficient parametrization also allows rapid numerical integration. The parametrized field should be continuous with a bounded second derivative, should be realistic within oceanographic expectations, and should be consistent with the input (measured or climatological) sound-speed data.

The use of cubic functions in depth to smoothly parametrize the data may lead to strong oscillation if the results are constrained to pass through the original data. This is due in part to the constraint of differentiability of the second derivative. This constraint is not strictly required to eliminate the spurious NTP caustics, which arise from an unbounded second derivative.

Quadratic polynomials in the vertical are used here, the minimum requirement to bound the second derivative. The second derivative may be discontinuous. This parametrization has been previously used to model layered structures (Pederson and Gordon, 1967; Weinberg, 1975). Horizontal layers are also used. The parametrization is thus composed of constant, linear, or parabolic sound-speed layers with matched values and matched derivatives at their boundaries. The parameters within each layer are allowed to vary laterally with range.

A sound-speed profile prescribed at depths $\hat{z}_i$ is denoted c_i, with $\hat{z}$ (equal to $-z$) increasing downward. Indices i also increase downward. A profile with a continuous piecewise first derivative and a finite piecewise constant (but discontinuous) second derivative can be constructed by convolving a top-hat function of width $2w$ and unit area with a continuous piecewise linear function c_L connecting the points. The convolution yields

$$c_Q(w;\hat{z}) = \frac{1}{2w}\int_{-w}^{w} c_L(\hat{z}-\hat{z}')dz'. \tag{13}$$

The result is a continuous piecewise parabolic function with a continuous piecewise first derivative and a finite piecewise constant (but discontinuous) second derivative. If the half-width w is less than the spacing between input points (knots), then c_Q will be parabolic for $\hat{z}$ within w of a knot and it will be linear and equal to c_L for all $\hat{z}$ that are not within w of a knot.

Generally, sound-speed profiles are more densely specified in the upper few hundred meters of the ocean, where the

variability is greater than beneath. The above method of parameterization can be generalized to let w vary with depth. If a set of w_i is constrained such that

$$\hat{z}_i - w_i \geq \hat{z}_{i-1}, \tag{14a}$$

$$\hat{z}_i + w_i \leq \hat{z}_{i+1}, \tag{14b}$$

then it is always possible to use these w_i to construct a continuous piecewise parabolic function $\hat{c}_Q$, with continuous first derivative, which is analogous to c_Q except for the use of variable w_i. This vertically parametrized sound speed is used in our calculations.

The functional forms of the piecewise quadratic sections of $\hat{c}_Q(\hat{z})$ depend on the overlap (if any) of the adjacent half-widths w_i. There are three cases, described in detail by Bowlin *et al.* (1993). Case 1 merely gives the linear segments of c_L away from $\hat{z}_i$. It occurs when $\hat{z}_{i-1}+w_{i-1}<\hat{z}<\hat{z}_i-w_i$. Case 2 reproduces the parabolic sections of $c_Q(w_i;\hat{z})$ near z_i. It occurs when $\max(\hat{z}_{i-1}+w_{i-1},\hat{z}_i-w_i)<\hat{z}<\min(\hat{z}_{i+1}-w_{i+1},\hat{z}_i+w_i)$. Case 3 is the smooth interpolation of two "overlapping" sections of case 2. It occurs for $\hat{z}$ such that $\hat{z}_{i+1}-w_{i+1}<\hat{z}<\hat{z}_i+w_i$. Note that case 3 or case 1 sections are sandwiched between two case 2 sections. Case 2 sections may connect.

The quadratic parametrizations do not pass through the original data set c_i,

$$\hat{c}_Q(\hat{z}_i) = c_i + w_i\alpha_i/4, \tag{15}$$

and have a different vertically averaged sound speed than the PWL interpolated input. If the half-widths of the smoothing regions w_i were much smaller than the spacing of the $\hat{z}_i$, then this effect would be small. However, it is desirable to eliminate the discrepancy for large w_i.

A solution is to find a new set of sound speeds $\tilde{c}_i$ that will produce a $\hat{c}_Q$ passing through the original c_i. These are obtained from the following set of linear equations:

$$c_i = \tilde{c}_i + \frac{w_i}{4}\left(\frac{\tilde{c}_{i+1}-\tilde{c}_i}{h_i} - \frac{\tilde{c}_i-\tilde{c}_{i-1}}{h_{i-1}}\right), \tag{16}$$

where $h_i=\hat{z}_{i+1}-\hat{z}_i$. This set of tridiagonal equations can be solved directly (Press *et al.*, 1986). Use of the exact solution can occasionally lead to pathological profiles if the w_i are allowed to overlap.

Figure 3 shows the resultant profiles generated from two parametrizations of Barents Sea $c(z)$ measurements, provided by J. Lynch. Sound speed was sampled at 10-m intervals. One profile uses a half-width of 4 m, giving 2-m linear sections between parabolic sections. The other profile uses half-widths $w_1=7$ m, with 4-m overlap, providing alternating case 2 and case 3 layers. The $w_i=4$ m profile more directly connects the points.

A small overshoot in the surface mixed layer is seen in the $w_i=7$ parametrization of the Barents Sea profile (Fig. 3). This behavior can be avoided and smoothness can be enhanced in two ways. First, w_i with no overlap can be used. Second, the constraint of passing through the original data can be removed, in a manner similar to that of the smoothing

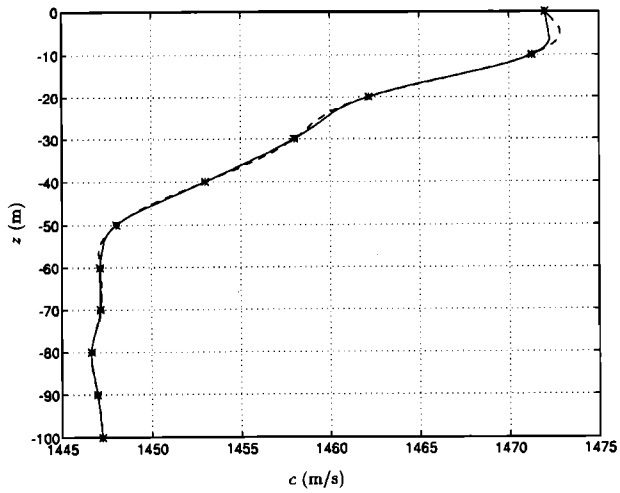

FIG. 3. The star symbols show 10-m samples of sound speed from the Barents Sea. Two parametrizations of sound speed produce the two continuous profiles. Half-widths of 7 m (dash), giving 4-m overlapping (case 3) parabolas between case 2 parabolas, show considerable overshoot in the upper mixed layer. Half-widths of 4 m (solid), giving 2-m linear (case 1) sections between parabolas, provide a better result for the mixed layer and less overall waviness in the profile. Increased curvature in the $w_i=4$-m model allows the profile to make sharper turns into the upper and lower isovelocity layers.

spline (Lancaster and Salkauskas, 1986). An iterative implementation of the second technique is possible (Bowlin *et al.*, 1993).

In this paper we utilize case 1 and case 2 parametrizations, with no overlapping parabolas. Table I contains the input data depths and three sets of w_i that are used.

Figure 4 shows the results of parametrizing a profile from the Levitus summer database at Slice89 location 34°N, 140°W in the North Pacific. The parametrized profiles use three sets of w_i listed in Table I, termed cases A, B, and C. The profiles pass through the input points, and they contain alternating linear and parabolic sections (except for the connected parabolas for case A near the surface). The smooth profiles have lower mean sound speeds than the PWL profile. In general, the smoother the profile of a refractive waveguide constructed from a discrete sample set, the slower the average sound velocity. For Slice89 range-dependent propagation, modeled in Sec. III, ray travel times computed using a case B parametrized environment average about 8 ms less than those using case A, and case C about 13.5 ms less than case A.

Sound speed must also be parametrized in range in a way that will not introduce artificial complexity into the wavefronts. It has been found that linear interpolation in range is sufficient to attenuate artifacts, that is, ray-tracing results are not sensitive to details of a linear parametrization, such as profile spacing. Interpolation between input profiles is made at fixed depth, after evaluating the parametrizations of the bracketing profiles at that depth. The ray equations depend upon c, $\partial c/\partial z$, and $\partial c/\partial r$, and these vary smoothly with range and depth in this parametrization, with the exception of discontinuous $\partial c/\partial r$ at each profile. If ray paths are sensitive to $\partial c/\partial r$, then this linear technique will contain modulations of wavefronts governed by the depths at which

TABLE I. The indices i and the depths at which sound speeds c_i are input to the parametrizations are listed. Components of the w vectors governing the case A, B, and C parametrizations are listed.

Index i	Input depth $\hat{z}_i$	Case A w_i	Case B w_i	Case C w_i
1	0	5	3	1
2	10	5	3	1
3	20	5	3	1
4	30	5	3	1
5	50	5	3	1
6	75	12	6	3
7	100	12	6	3
8	125	12	6	3
9	150	12	6	3
10	200	25	13	6
11	250	25	13	6
12	300	25	13	6
13	400	50	25	13
14	500	50	25	13
15	600	50	25	13
16	700	50	25	13
17	800	50	25	13
18	900	50	25	13
19	1000	50	25	13
20	1100	50	25	13
21	1200	50	25	13
22	1300	50	25	13
23	1400	50	25	13
24	1500	50	25	13
25	1750	50	25	13
26	2000	125	63	31
27	2500	125	63	31
28	3000	250	125	63
29	3500	250	125	63
30	4000	250	125	63
31	4500	250	125	63

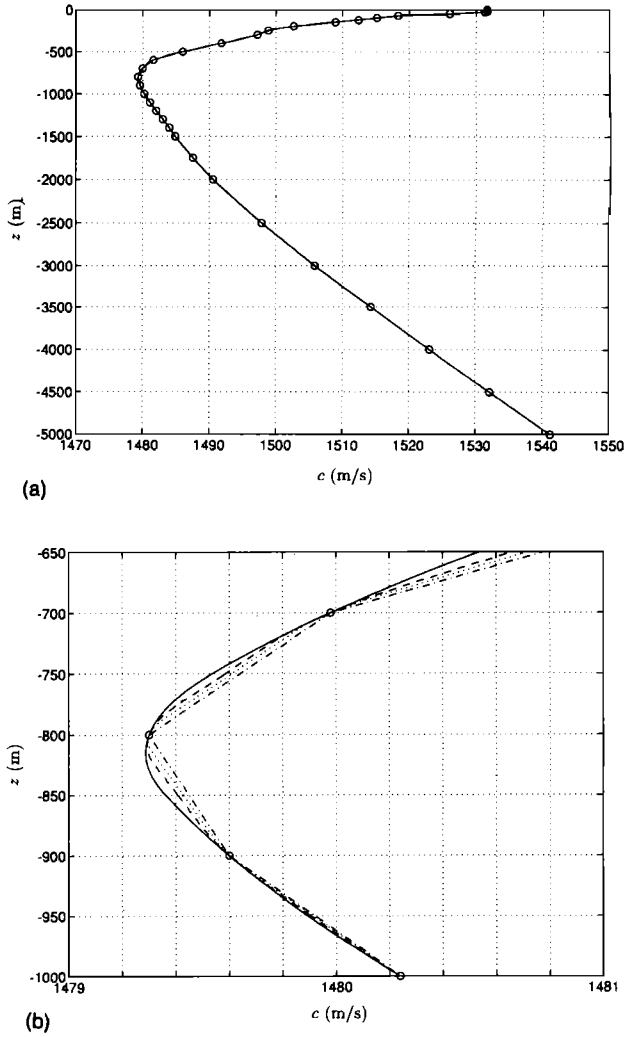

FIG. 4. (a) A parametrized profile is shown, fitting the summer Levitus data (circles) from 32°N, 150° W in the North Pacific, near the Slice89 transmitter. (b) An expanded view of four parametrized profiles compares case A, B, and C parabolic/linear parametrizations with a PWL model (rightmost line, dash–dot). Results of cases A (solid), B (dash), and C (dot) have lower depth-averaged sound speeds than PWL, with the difference depending on w_i. A continuum of profiles with varying w (and smoothness) will fit the available data, each with a different mean, forming an infinite profile set consistent with the data. The PWL model is clearly inappropriate because it contains high-wave-number components not resolved in the data.

rays pass through the interfaces. The modulations were not observed to occur; therefore this term is not important for the region of the ocean modeled here.

C. NTP caustic dependence on systematically related channels

Detailed ray investigation of 1000-km propagation is consistent with observations because Slice89 timefronts were stable for early arriving energy (Fig. 1). The early timefronts had roughly 6–11-ms rms time variability or wiggliness (Duda *et al.*, 1992) and some intensity variability. Scintillation indices, σ_I^2 (Fante, 1975), vary from about 0.2 to 2.0 for individual identified timefront arrivals measured as time series at distinct depths, with an average of about 0.9. However, as with a previous 1000-km experiment (Dushaw *et al.*, 1993), distinct timefronts were only identifiable in the early portion of the pulse. The stability of the early arrivals lends credibility to a geometric-ray study of wavefront propagation at 1000-km range.

Figure 5 shows late portions of arrival patterns for rays traced through profiles parametrized from the summer Levitus database (Levitus, 1982). The single set of discrete input profiles used for all simulations in this section were interpolated from the Levitus horizontal grid at 100-km intervals along the propagation path. Four thousand rays, at equal launch-angle intervals between $-15°$ and 15°, were calculated. Figure 5(a) shows timefronts calculated using the set of largest w_i in Table I (case A). Figure 5(b) shows timefronts calculated using smallest w_i, case C.

The early portions (arrival time before 676 s) were virtually identical in shape for the two runs, except for a few triplications along vertically inclined timefront segments. The timefronts diverge in the displayed later pulse portion. The case C pattern is more complex at the end, with overlapping timefronts. The complicated overlapping near 676.33 and 676.40 s is associated with high $\partial_{zz}c$ at upper turning points near 600 and 700 m. The case C simulation has a longer, narrower tail of near-axial energy because of the sharper sound-speed minimum. The vertical distribution of received energy appears to be significantly broadened in experiments compared to these simulations.

Since varying the smoothing parameters w_i has a pro-

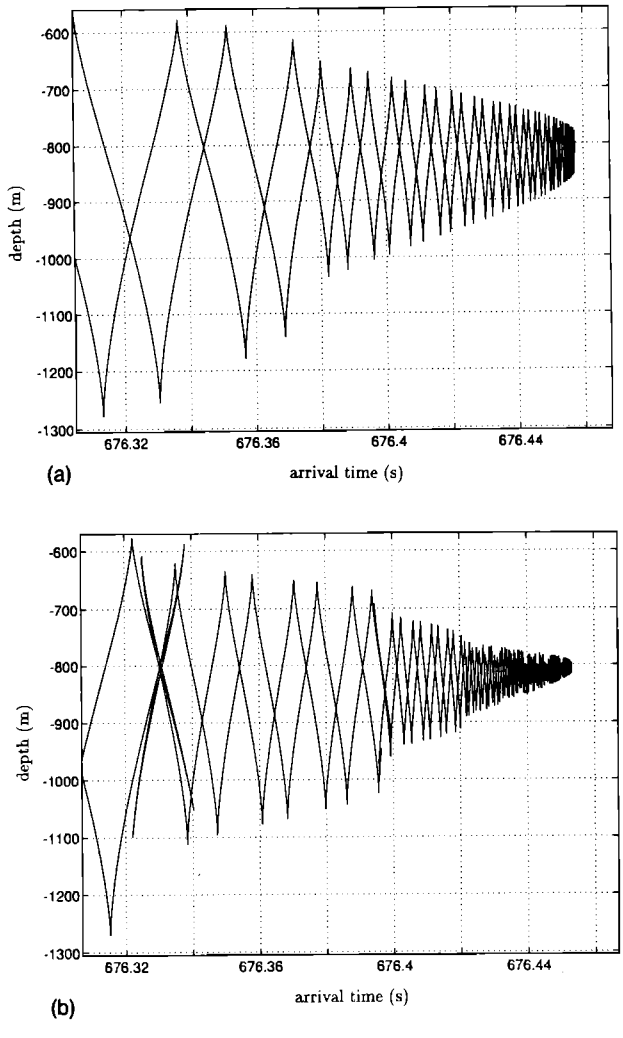

FIG. 5. (a) The late-arriving end of a Slice89 pulse, modeled using a range-dependent case A parametrized set of Levitus profiles, contains ever-closer timefronts as it approaches the axial-energy limit. (b) The same section of the Slice89 pulse modeled using the case C weights, instead of case A, has extra folded timefront sections. The sharp jumps in the envelope of the timefront, joined by regions of extra timefront segments and caustics, are artifacts of the choice of input sampling depths. Those depths determine the locations of the linear and parabolic sound-speed sections and thus the timefront geometry.

nounced effect on the second derivative of c, we evaluate timefront effects in terms of U. Figure 6 shows histograms of $\log_{10}|U|$ values for the parametrized summer Levitus profiles, using w_i of cases A, B, and C (Table I). Only the U that satisfy $0.01<|U|$ are utilized in the histograms, which includes virtually all of the curved sections of the profile. Also, only concave portions of the profiles are used, with sound speed accelerating with vertical distance from the axis, since these features were observed to cause triplications in our simulations. Convex portions have not been included because their effect has not yet been examined, although they probably also contribute to wavefront complexity. Including the linear profile sections (where $U=0$) in this analysis would preclude the use of the logarithm, obscuring the analysis of the highly skewed distribution. Statistics of U do not exist rigorously since U is unbounded, but we analyze the bounded subset of U to arrive at approximations. The density functions shift toward higher $\log_{10}|U|$ as w_i are reduced. The mean $\log_{10}|U|$ values are 1.43 for case A, 1.75 for case B, and 2.05 for case C. For comparison, the smooth analytic Munk profile (Munk, 1974; Smith *et al.*, 1992a, 1992b) has a mean $\log_{10}|U|$ of 1.14.

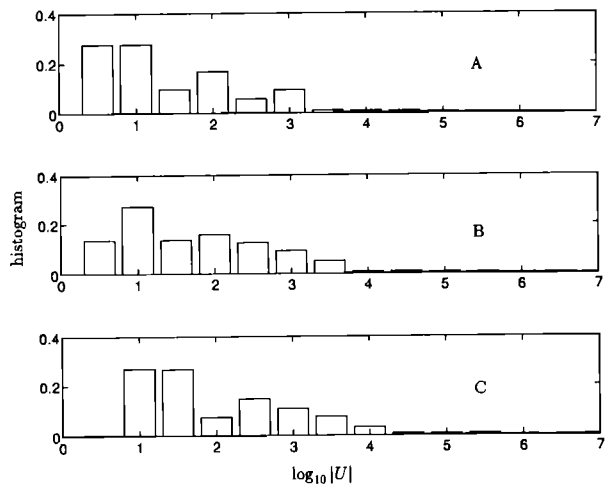

FIG. 6. Histograms of $\log_{10}|U|$ indicate how the distribution of $|U|$ changes for different parametrizations. The units of the ordinate are quantity in each bin divided by the total number of samples, approximating the probability density function. The case A parametrization of the summer Levitus Slice89 profiles gives few $|U|$ values above 1000 (top frame), in contrast with cases B and C (bottom).

Figures 7 and 8 show results of varying the half-widths w_i. Case A, B, C, and PWL parametrizations were applied to

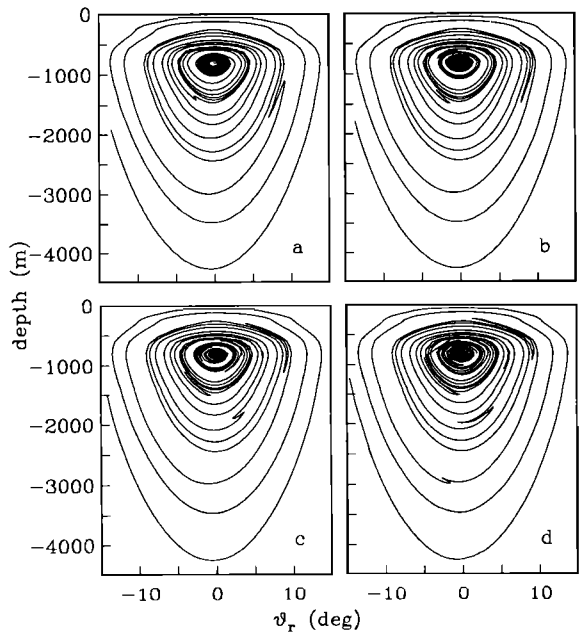

FIG. 7. Spiral diagrams of the arrival-angle, arrival-depth locus show the gradual increase of NTP caustic/triplication effects, shown by zigzags, as curvature in the parametrizations is increased. Results are from rays traced through four parametrizations of a single set of input sound-speed profiles from the Slice89 region; case A is shown in (a), case B in (b), case C in (c), and PWL parametrization in (d). Results for 2000 positive launch angles between 0° and 15° are plotted, connected by continuous lines. The outermost winding is the highest launch angle. The number of zigzags grows through the sequence, from (a) to (d), as does the size of directly comparable zigzags.

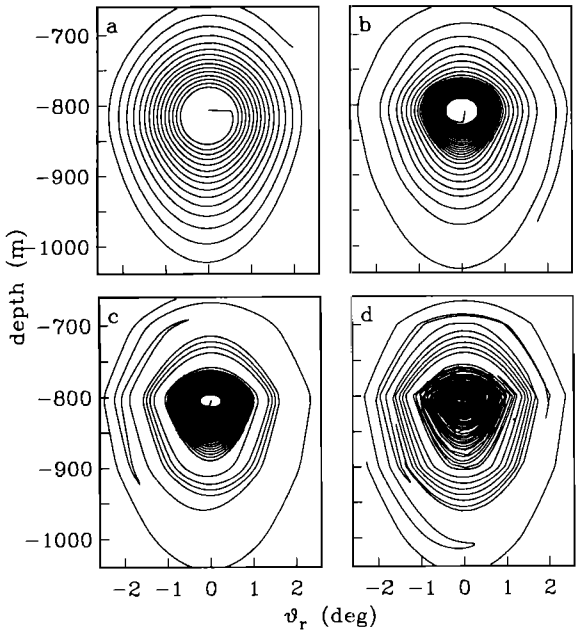

FIG. 8. Expanded views of the centers of the Fig. 7 spirals show the successive increase of caustics when the cases A, B, C, and PWL ray traces are compared. The frame order is the same as Fig. 7. Results for 3000 positive launch angles between 0° and 2.5° are plotted, connected by continuous lines. A large wavefront reversal extends from 2°, −800 m to 0°, −1000 m in (d). The sharper and shallower sound-speed minima for cases B, C, and PWL are nearer the source depth at 804 m, giving more late low-angle rays in the center.

the set of Levitus input profiles. Wavefront reversals and triplications are seen on the arrival-angle/arrival-depth diagrams for all four cases. The zigzags along the angle/depth diagrams gradually increase as the w_i are decreased. This corresponds to more acoustical energy in reversed wavefronts. The effect of reducing w, and thus increasing curvature, is the enhancement of the triplications and caustics.

Figure 9 is an expansion of a portion of Fig. 7 showing

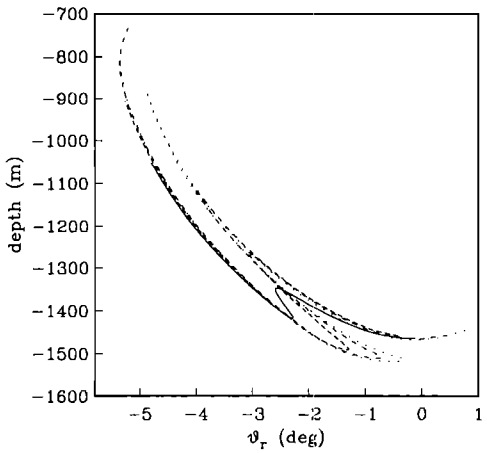

FIG. 9. An expanded view of portions of the curves in Fig. 7 shows the sensitivity of one particular wavefront triplication to parametrization-controlled curvature changes. The case A curve is shown as a solid line, case B is shown as a broken line extending to −1.3° in its lower turn, case C is the more broken line turning at −0.8°, and the PWL curve is dotted, turning at −0.3°. The case A triplication covers the smallest extent of angle and time. The triplication encompasses greater depth and angle as the w_i are systematically reduced, that is, when U values are systematically increased.

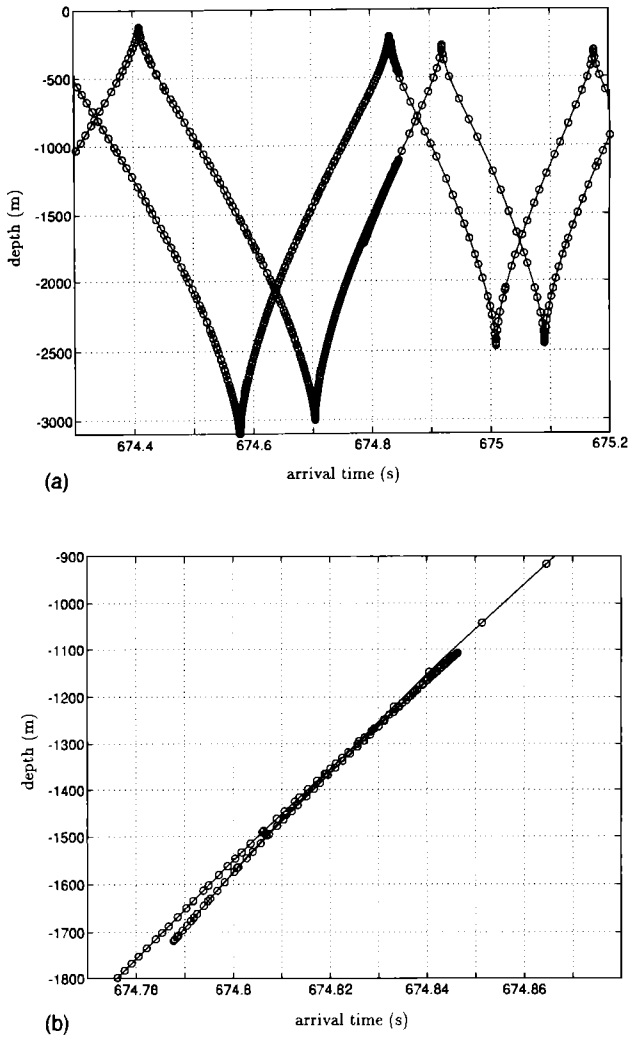

FIG. 10. (a) A timefront triplication depicted in Fig. 7(a) (case A parametrization) is shown in arrival time/depth coordinates at 1500 m, 674.8 s. Another triplication for negative initial angle energy is evident at 400 m depth, at the same time. (b) An expanded view of the triplication shows that the timefronts are separated in time by a maximum of 5 ms. The circles indicate the individual calculated ray arrivals.

the effect of the curvature on a single triplication centered at 1400 m depth and −2.5° arrival angle. Figure 10 shows the associated portion of the timefront for the case A parametrization. The reversed timefront has virtually the same arrival time as the normal portions over much of its extent, and is never separated by more than 5 ms. Much of the overlapping energy would coherently sum for low-frequency signals, and would be difficult to resolve in a band-limited experiment. Instead, paired caustics would appear, consistent with the intense regions labeled NTPC in Fig. 2.

Reversal of wavefronts is shown by graphs of S for a small set of launch angles ψ [Fig. 11(a)], where S is the derivative with respect to ψ of horizontal velocity between the source and a specified range. One significant difference between S and S_1 is that S has structure associated with ray turning points near the receiver range, and S_1 does not. For case A, S is usually negative for these negative ψ, with one exception at about −9.5° where there is a triplication [Fig. 10(a), top], although there are prevalent spikes approaching zero. The positive S feature is stable with respect to ψ and

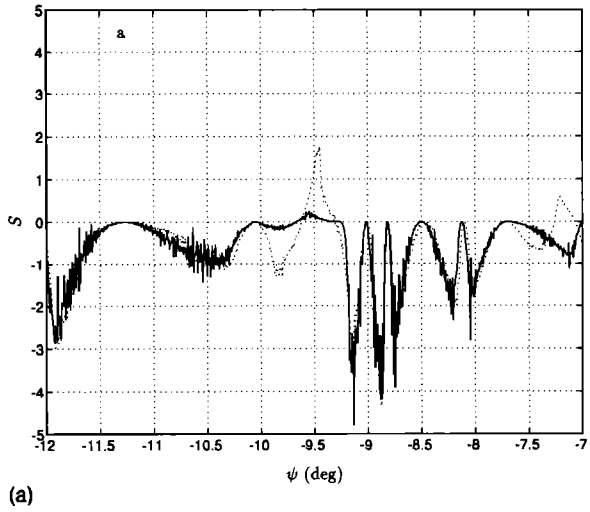

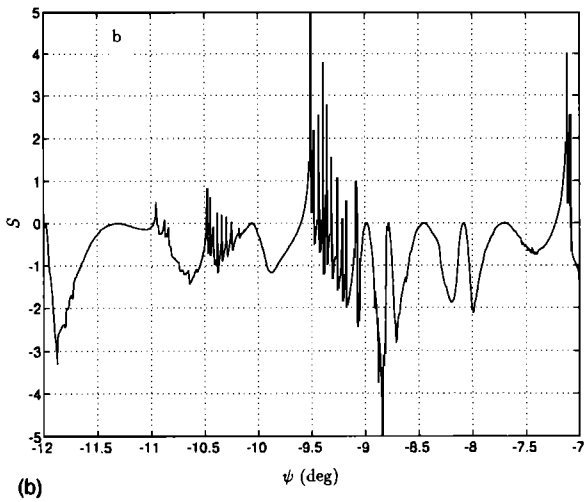

FIG. 11. (a) S, estimated by first-difference of group velocity with respect to ψ, is shown for the shallow triplication of Fig. 10(a). The solid line shows the result for the case A simulation [the timefront at the top of Fig. 10(a)], and the dotted line the result for case C. The curves rise to zero at wavefront vertices, such as in Fig. 5(a), but become positive, indicating a reversed wavefront, at about $\psi = -9.5°$. Paired NTP caustics occur where the curves cross zero. (b) The first differences for the PWL wavefront show many NTP caustics and wavefront reversals.

traverses 0.5°, representing a significant fraction of radiated energy. Case C results in a greater change in group velocity in this feature, giving a physically longer reversed rangefront, but the feature involves about the same range of ψ. For comparison, Fig. 11(b) shows that the PWL result has many NTP caustics and reversals. Although individual case C reversals do not always take up more radiated energy than their direct case A counterparts, a higher fraction of total case C energy is contained in reversals since they are more prevalent. Figure 12 shows the percentages of ψ between $-15°$ and 15° that make up the reversed wavefronts. The percentage rises as mean $\log_{10}|U|$ is changed via w_i.

An additional effect is an overall shift in arrival time of a few milliseconds, discussed in Sec. II E. Since details of the triplications are sensitive to the depths of the high-curvature sections, the most reliable deterministic predictive calculation is judged to be that using the case A (widest w_i). That result has the fewest triplication features, and is least sensitive to the input grid and the profile of U. The high-U

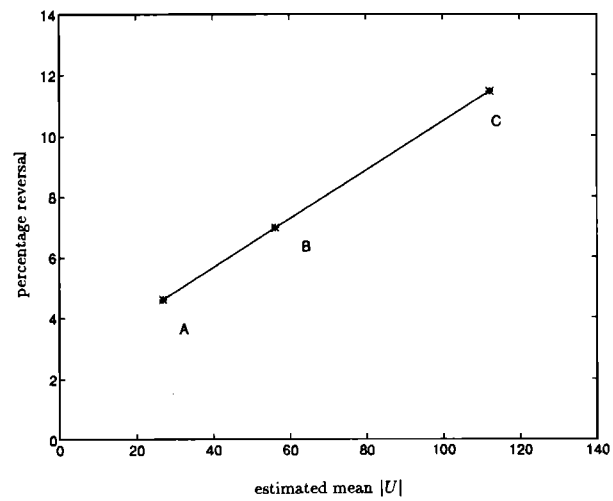

FIG. 12. The percentage of reversed timefront for the case A, B, and C simulations increases with U. The abscissa is 10 raised to the power mean $\log_{10}|U|$. The percentage is computed over launch angle ψ. The middle leg of the triplication of Fig. 10(b) is an example of what is termed a reversed timefront.

effects are not accurately predictable because of hydrographic sampling insufficiencies and intrinsic temporal fluctuation of the ocean at small scales.

D. Intensity variation from paired caustics and wavefront stretching

For a single continuous rangefront emanating from a source, relative intensity along the rangefront (or timefront) can be approximated by the initial angular extent of a ray group divided by the distance that the arriving ray group spans. This is the ray density technique used in seismology (Lay and Kanamori, 1985; Woods and Okal, 1987) and is consistent with energy conservation within ray tubes. Since the arriving energy is approximately horizontal, the vertical distance is used. If two rays initialized at a specific angular separation are considered, the intensity of the front between two arriving rays is approximately proportional to the inverse of their vertical arrival separation, provided no reversals (caustics) are included in the front segment.

Log intensities for the case A and C simulations are shown in Fig. 13 for a subset of the ψ plotted in Fig. 11. The associated timefronts, each showing a pair of NTP caustics, are shown in Fig. 14(a). There is an alteration of intensity beginning at the fourth dot (75th ray) from the left, which is in the vicinity of the first NTP caustic at about $-9.6°$. The intensities become similar again to the right of the second NTP caustic at -9.3 s. The intensities at the caustics cannot be calculated in this manner (Brekhovskikh, 1980).

There are three causes of intensity fluctuation. The first two are closely related. First, focusing of energy at the caustics leads to intensification. Second, stretching or contraction which must accompany the folding may extend along the timefront, either increasing or reducing intensity. Third, the closeness of folded timefronts (Fig. 10) may lead to coherent addition of energy at finite frequency, with increase of observed intensity. For finite frequency propagation, the fold

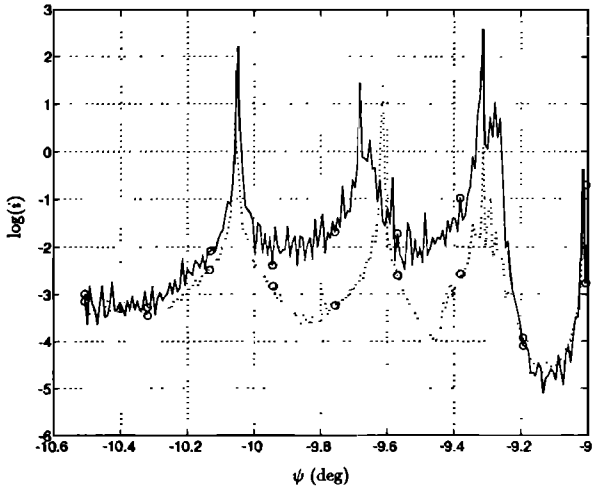

FIG. 13. The log-intensity for short portions of the case A and case C timefronts, normalized by the mean intensity, shows considerable variability. Case A is the solid line. Intervals of 25 launched rays (or 0.1875° ψ intervals) are indicated with circles. The intensity changes are linked to expansion or contraction of the timefront in the vicinity of reversals, induced by the small differences between the A and C profiles. The high-intensity spike at −10.05° is the stable, macroscopic turning-point caustic, while the two at about −9.65° and −9.3° are NTP caustics.

may perhaps be better considered as an intense caustic region. Many intense timefront portions were observed in Slice89 (Fig. 1).

E. Timing variation from sound-speed curvature

Rays calculated using different parametrizations give different timefront shapes and arrival times. There are two effects. The first is variability localized in small parts of the wavefront, near reversals and triplications. The second is timing variability extending over large portions of the wavefront, a weakly ψ-dependent effect but not a true bias.

Figure 14(a) shows the portion of the timefront calculated over the same range of ψ used in Fig. 13. Timefronts from cases A and C are shown. The circles mark intervals of 25 rays, or ψ increments of 0.1875°. In the vicinity of the reversal, at ψ−9.6°, the arrival times for equal launch angles vary by up to 80 ms [Fig. 14(b)]. However, if the timefront shapes are compared with no regard to ψ, then most of the timefront from case A lags the case C timefront by about 13 ms. Except for this bias-like effect of the lower sound speeds of the smoother case A profile [Fig. 4(b)], there are no large geometric changes in the timefront. The localized timefront distortions seem to slide essentially parallel to a robust, fixed geometrical shape. The local timing variations between legs of triplications appear to be less than 5 ms in magnitude for 1000-km propagation.

Figure 15 compares the case A front with a shifted version of the case C front. They align well for long stretches, but the difference makes abrupt jumps at the triplications. Two comparable triplications exist for each case, but are difficult to see in the dotted timefront. The constant offset (or bias) represents an uncertainty attributable to vertical undersampling of the concave sound-speed profile. This uncertainty cannot be eliminated without immense quantities of

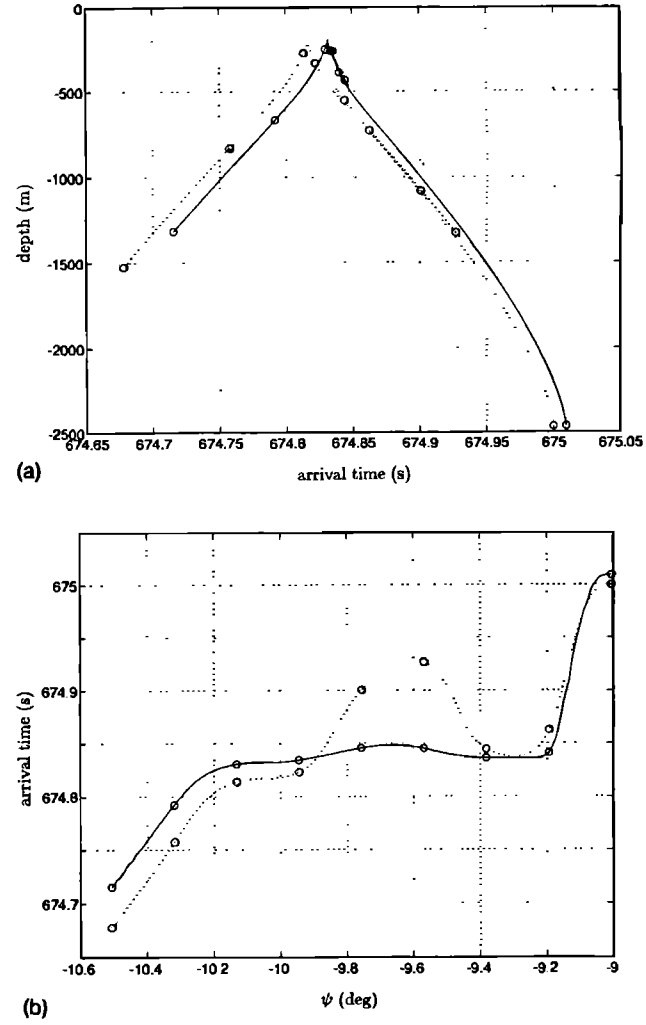

FIG. 14. (a) The case A (solid) and case C (dot) timefronts calculated for the launch angles of Fig. 13 show a very similar shape, with the exception of the triplications. The circles indicate the same index rays as Fig. 13. The 13.5-ms offset between the two timefronts is the most distinct difference. (b) The difference in arrival time at each of these launch angles can reach 80 ms as the timefront folds or contracts. The index rays are as in (a). The stable portion of the timefront (ψ<−10°) shows the steady offset, which is greater when measured at constant ψ than the visual offset shown in (a) because of differing timefront geometry. The larger offsets occur near triplications.

data. It is smoothly varying along the timefront and is reduced for earlier arrivals which spend a greater fraction of their time in the deep portion of the sound channel, where $c(z)$ from the three parametrizations varies little.

III. STOCHASTIC FINESCALE CURVATURE STATISTICS

Mesoscale or larger sound-speed gradient and curvature features vary over periods of a week to years, and cannot be fully measured. These have been shown to give small-scale wavefront distortion (tens to hundreds of meters). These are accompanied by finescale ocean features. Both static and dynamic thermohaline finestructures complicate the sound channel. The static finestructure may consist of layers containing interleaved water masses of different origins, such as profiles through a Mediterranean salt lens or in the vicinity of a front. The dynamic finestructure is primarily induced by

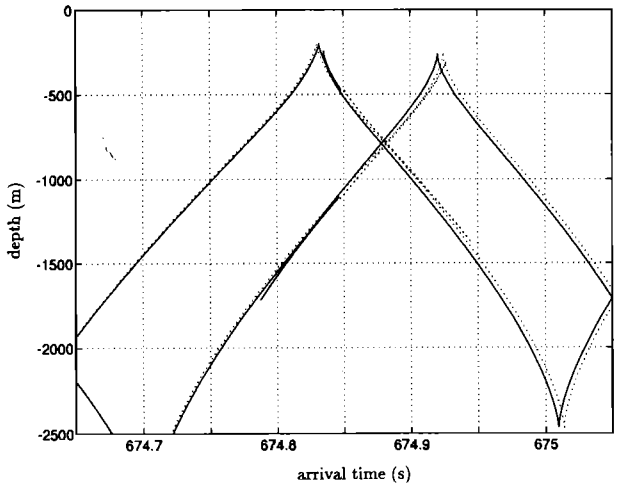

FIG. 15. The case A timefront (solid) aligns well with a shifted version of the faster case C timefront. An offset of 13.5 ms is added to the case C front. Only a portion of the timefront is shown, but the displacement persists over most of the front. The displacement is not precisely constant, and makes its greatest shifts near triplications, seen between 674.8 and 674.9 s in both timefront sections.

vertical strain from internal gravity waves at periods shorter than one day (Flatté, 1983; Flatté *et al.*, 1979; Munk and Zachariasen, 1976b).

Figure 16 shows one measured profile from the Slice89 experiment (Cornuelle *et al.*, 1993; Worcester *et al.*, 1993). The base 10 logarithm of $|U|$, calculated from first and second differences over 2-m spacing, is also shown. $|U|$ exceeds 10^6 regularly, and in regions at and just below the sound-channel axis its local mean is approximately 10^5.

The Garrett–Munk (GM) spectral model of internal waves (Garrett and Munk, 1975; Gregg and Kunze, 1991) can be used to model the dynamic stochastic behavior of U. This model of the wavenumber-frequency spectrum is vertically symmetric, horizontally isotropic, consistent with the linear internal-wave dispersion relation, and separable in wave number and frequency. The modeling technique uses

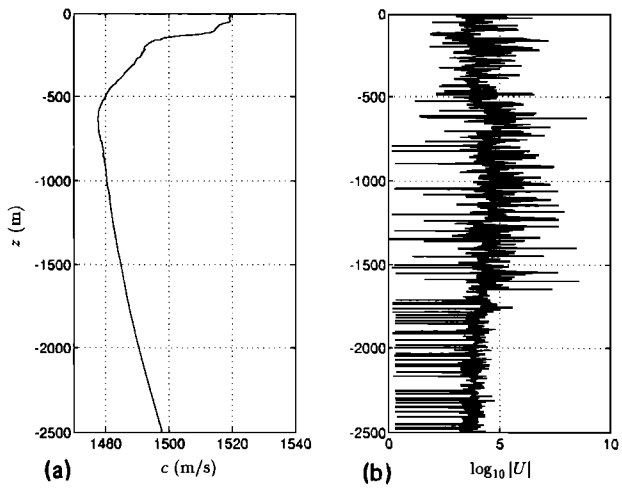

FIG. 16. (a) One hydrographic profile from the Slice89 experiment shows small-scale structure. (b) The base-10 logarithms of $|U|$ are much greater in the data than in the case A, B, and C parametrizations (Fig. 6).

random series of internal wave displacement η, vertical strain $\partial_z \eta$, and vertical derivative of strain $\partial_{zz} \eta$ generated at a sequence of depths. Each member of each series is a Fourier summation of vertical waves, with amplitudes taken from GM vertical wave-number spectra of each of the three quantities (Gregg and Kunze, 1991). The spectra vary with the buoyancy frequency, essentially the density gradient, which varies with depth. Wave numbers from 0.0005 to 0.1 cycle/m were used. Series of 200 random phases were used to generate the spectral components, repeated 1000 times at each depth, giving 1000 realizations of η, and its derivatives, at each depth. The same phases are used for all three quantities at each depth, so that η and the derivatives have the correct relation. Both the density profile and the sound speed profile are taken from the Levitus summer temperature and salinity profiles at the Slice89 source.

To compute statistics of U from the modeled wave quantities, the sound speed is broken down into background and fluctuating terms,

$$c(z) = c_0(z) + c_f(z). \tag{17}$$

The mean value of U can then be expressed as

$$\langle U \rangle = \left\langle \frac{c_0 \partial_{zz}(c_0 + c_f)}{\partial_z^2 (c_0 + c_f)} \right\rangle, \tag{18}$$

where c has been approximated with c_0 in the numerator. The background c_0 and its derivatives are evaluated from an eighth-order polynomial fit to the discrete Levitus profile. The fluctuation components can be directly evaluated from c_0 and the internal-wave parameters. The fluctuation is equal to the potential sound-speed gradient $\partial_z c_p$ times the displacement,

$$c_f = \eta(\partial_z c_0 - \gamma_A) = \eta \, \partial_z c_p, \tag{19}$$

where γ_A is the adiabatic sound-speed gradient (Munk and Zachariasen, 1976b). Differentiation gives

$$\partial_z c_f \approx \eta \, \partial_{zz} c_0 + \partial_z \eta \, \partial_z c_p, \tag{20}$$

because γ_A is approximately constant. Another differentiation gives

$$\partial_{zz} c_f = \eta \, \partial_{zzz} c_0 + 2 \, \partial_z \eta \, \partial_{zz} c_0 + \partial_{zz} \eta \, \partial_z c_p. \tag{21}$$

Specification of the profile c_0 and γ_A are thus sufficient to compute the required quantities from η, $\partial_z \eta$, and $\partial_{zz} \eta$.

Figure 17 compares the mean of measured values of $\log_{10}|U|$, rather than $\langle U \rangle$, with modeled values as a function of depth. The random series of $|U|$ are highly skewed, visually similar to exponential or log-normal, but their distribution has not been rigorously examined. In the data evaluations, $|U|$ values exceeding 10^8 are excluded. These are points where $\partial_z c$ is near zero. Statistics of U or functions of U do not exist rigorously because of this behavior. Because of the skewness, rms values are not estimated.

The profile of mean $\log_{10}|U|$ predicted from the spectral model of deep-ocean internal waves agrees with observation in the Slice89 area. There is some disagreement near the surface, where static finestructure contributions (Desaubies and Gregg, 1981) could account for some of the surplus in the observations. In addition, some disagreement is reason-

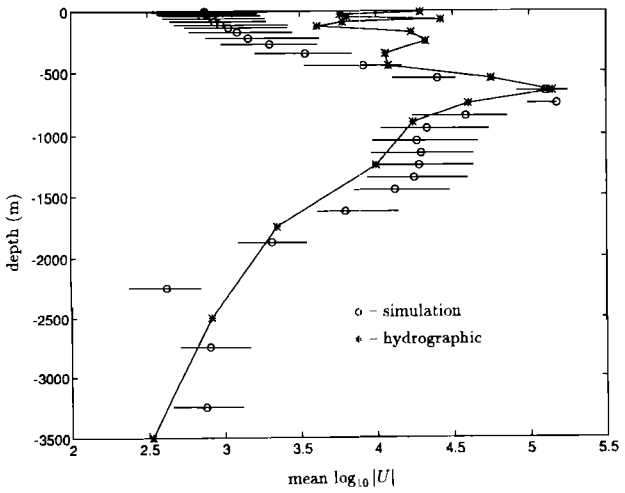

FIG. 17. Statistics of simulated U using vertical displacements, strains and derivatives of strains consistent with the Garrett–Munk internal-wave model are comparable with those from 12 Slice89 CTD casts (Cornuelle *et al.*, 1993). The Slice89 data are shown as *'s. Mean $\log_{10}|U|$ is highest at the sound channel minimum, where the derivative of c_0 is zero. Mean $\log_{10}|U|$ is calculated within vertical bins from the data, and computed at a selection of depths in the simulation. The values simulated with the GM energy level are indicated by O's. The lateral lines connect additional simulations at one-third and three times the GM internal-wave energy, indicating a range of probable natural variability.

able since the GM spectrum has been observed to not precisely fit data from shallow depths (Pinkel, 1984).

The mean of $\log_{10}|U|$ is highly depth-dependent, with maximum at the sound channel minimum where the mean gradient is zero, as expected. Wavefront segments associated with ray turning points near the minimum, the late-arriving axially trapped energy, are most susceptible to the U-dependent folding and timing fluctuations studied in Sec. II. This is a possible reason for the lack of reproducible, separable, identifiable timefronts in the middle and late portions of two experimental Pacific arrival structures (Worcester *et al.*, 1994; Dushaw *et al.*, 1993).

IV. SUMMARY

Simulating wavefronts with closely spaced rays shows that systematically increasing the relative curvature parameter U enhances wavefront triplication. Repeated simulations over closely related sound channels were used to quantify the effect, with all channels fitting a single set of input data but having different distributions of U. Most of and perhaps all of the effect can be explained by high U at ray turning points. The triplications cause intensity and timing (phase) fluctuations. Timing differences between triplication legs are less than 10 ms at 1000-km range in our simulations. Figure 2 shows an observed triplication similar to our simulated ones, suggesting that ray-derived effects of high U are similar to actual propagation effects at 250 Hz. That figure also shows some high-intensity regions of the timefronts that are consistent with unresolved NTP caustics and triplication, expected at finite frequency.

It is probable that U in the ocean is dominated by stochastic fluctuations. This means that any lack of predictability from poor spatial resolution, with resultant uncertainty in U, is accompanied by temporal unpredictability. The mean logarithm of $|U|$ (or a quantity we analyze as if it were such, since unboundedness of U creates difficulties) increases near the sound-speed minimum for both actual data and an internal-wave fluctuation model. The mean oceanic $\log_{10}|U|$ value is much greater than that used in our simulations, especially near the sound-speed minimum, implying strong effects for energy trapped near the sound-speed minimum. The depth dependence of the effect, implicit because mean U is depth dependent and is most influential at turning points, is consistent with observations of unresolved axially trapped energy. Parabolic equation simulations of propagation through similar high-U structure (Colosi *et al.*, 1994) show wavefront features reminiscent of the features shown here. The wavefront distortions of that study were stronger in the later part of the pulse, trapped near the channel axis where high U is more common. The effect of high U at turning points is a possible diagnostic explanation of those results.

There are a few secondary issues and results. One is the lack of predictability of propagation for climatic data, at least for frequencies where ray modeling is valid, perhaps above 100 Hz. Travel-time changes of tens of milliseconds can result from smoothing operations on the poorly resolved climatic vertical profiles. This uncertainty of travel time from mean structures is due to small-scale mean sound-speed profile components that are not adequately known or resolved, especially at the sound-speed minimum. Stated another way, the undersampled data do not sufficiently constrain the sound channel to enable precise prediction. This uncertainty would exist without the added complication of mesoscale or gyre-scale variations, which contribute error to the estimated climatic field. A second issue is the existence of NTP caustics in finite-frequency experimental wavefronts. If the multiple wavefronts are not resolved, these can appear as intensity fluctuations such as those seen in the experimental timefronts (Fig. 1). This is a process of intensity variation not entirely consistent with perturbation analyses of intensity. Third, analysis of NTP caustics depends upon eliminating the jumps in sound-speed gradient from the PWL approximation. This has been accomplished without adding spurious oscillations to the profiles by mixing quadratic and linear parametrizations.

This wavefront predictability analysis of vertical structure is complementary to recent ray chaos analysis in range-dependent environments (Smith *et al.*, 1992a, b). Different methods have been utilized, and that work suggests chaos, or limited predictability of a deterministic process if initial conditions are unknown even infinitesimally. However, implied unpredictability is common to both studies.

ACKNOWLEDGMENTS

This work was supported by the Office of Naval Technology (N00014-90-C-0098) and the Office of Naval Research, Ocean Acoustics Program (N00014-92-J-1162). J. Spiesberger and L. Freitag provided the climatological information and software. The calculations in Sec. I were developed in conversation with E. Terray. We thank J. Lynch for

the Barents Sea data. The Slice89 environmental data were collected and distributed by J. Boyd. This is WHOI contribution number 8546.

Boden, L., Bowlin, J. B., and Spiesberger, J. L. (**1991**). "Time domain analysis of normal mode, parabolic, and ray solutions of the wave equation," J. Acoust. Soc. Am. **90**, 954–958.

Bowlin, J. B., Spiesberger, J. L., Duda, T. F., and Freitag, L. F. (**1993**). "Ocean acoustical ray-tracing software RAY," Woods Hole Oceanographic Institution, WHOI Tech. Report 93-10, Woods Hole, MA.

Brekhovskikh, L. M. (**1980**). *Waves in Layered Media* (Academic, New York), 2nd ed.

Brown, M. G., Munk, W. H., Spiesberger, J. L., and Worcester, P. F. (**1980**). "Long-range acoustic transmission in the Northwest Atlantic," J. Geophys. Res. **85**, 2699–2703.

Colosi, J. A., Flatté, S. M., and Bracher, C. (**1994**). "Internal-wave effects on 1000-km oceanic acoustic pulse propagation: Simulation and comparison with experiment," J. Acoust. Soc. Am. **96**, 452–468.

Cornuelle, B. D., Worcester, P. F., Hildebrand, J. A., Hodgkiss, W. S., Jr., Duda, T. F., Boyd, J., Howe, B. M., Mercer, J. M., and Spindel, R. C. (**1993**). "Ocean acoustic tomography at 1000-km range using wavefronts measured with a large vertical array," J. Geophys. Res. **98**, 16 365–16 377.

Dashen, R., Flatté, S. M., and Reynolds, S. A. (**1985**). "Path-integral treatment of acoustic mutual coherence functions for rays in a sound channel," J. Acoust. Soc. Am. **77**, 1716–1722.

Desaubies, Y., and Gregg, M. C. (**1981**). "Reversible and irreversible fine-structure," J. Phys. Oceanogr. **11**, 541–556.

Duda, T. F., Flatté, S. M., Colosi, J. A., Cornuelle, B. D., Hildebrand, J. A., Hodgkiss, W. S., Jr., Worcester, P. F., Howe, B. M., Mercer, J. M., and Spindel, R. C. (**1992**). "Measured wavefront fluctuations in 1000-km pulse propagation in the Pacific Ocean," J. Acoust. Soc. Am. **92**, 939–955.

Dushaw, B. D., Worcester, P. F., Cornuelle, B. D., and Howe, B. M. (**1993**). "On equations for the speed of sound in seawater," J. Acoust. Soc. Am. **93**, 255–275.

Fante, R. L. (**1975**). "Electromagnetic beam propagation in turbulent media," Proc. IEEE **63**, 1669–1692.

Flatté, S. M. (**1983**). "Wave propagation through random media: Contributions from ocean acoustics," IEEE Proc. **71**, 1267–1294.

Flatté, S. M., Dashen, R., Munk, W. M., Watson, K. M., and Zachariasen, F. (**1979**). *Sound Transmission Through a Fluctuating Ocean* (Cambridge U.P. Cambridge).

Flatté, S. M., Reynolds, S. A., and Dashen, R. (**1987**). "Path-integral treatment of intensity behavior for rays in a sound channel," J. Acoust. Soc. Am. **82**, 967–972.

Flatté, S. M., and Stoughton, R. B. (**1986**). "Theory of acoustic measurement of internal wave strength as a function of depth, horizontal position, and time," J. Geophys. Res. **91**, 7709–7720.

Flatté, S. M., and Stoughton, R. B. (**1988**). "Predictions of internal wave effects on ocean acoustic coherence, travel-time variance, and intensity moments for very long-range propagation," J. Acoust. Soc. Am. **84**, 1414–1424.

Garrett, C. J. R., and Munk, W. H. (**1975**). "Space-time scales of internal waves: A progress report," J. Geophys. Res. **80**, 291–297.

Gregg, M. C., and Kunze, E. (**1991**). "Shear and strain in Santa Monica Basin," J. Geophys. Res. **96**, 16 709–16 719.

Henyey, F. S. (**1989**). "Why eddy diffusivity doesn't work," in *Proceedings of the 'Aha Huliko'a Hawaiian Winter Workshop*, edited by P. Müller and D. Henderson (University of Hawaii, Honolulu, Hawaii), pp. 245–249.

Lancaster, P., and Salkauskas, K. (**1986**). *Curve and Surface Fitting: An Introduction* (Academic, London).

Lay, T., and Kanamori, H. (**1985**). "Geometric effects of global lateral heterogeneity on long-period surface wave propagation," J. Geophys. Res. **90**, 605–621.

Levitus, S. (**1982**). "A Climatological Atlas of the World Ocean," NOAA Prof. Pap. 13, Princeton, NJ.

Müller, P., Holloway, G., Henyey, F., and Pomphrey, N. (**1986**). "Nonlinear interactions among internal gravity waves," Rev. Geophys. **24**, 493–536.

Munk, W. H. (**1974**). "Sound channel in an exponentially stratified ocean, with application to SOFAR," J. Acoust. Soc. Am. **55**, 220–226.

Munk, W. H., and Wunsch, C. (**1979**). "Ocean acoustic tomography: A scheme for large-scale monitoring," Deep Sea Res. **26A**, 123–161.

Munk, W. M., and Zachariasen, F. (**1976a**). ' "Reply to "Comments on 'Sound propagation through a fluctuating stratified ocean: Theory and observation,' " John J. McCoy, J. Acoust. Soc. Am. **60**, 1216–1217 (1976)," ' J. Acoust. Soc. Am. **60**, 1217–1218.

Munk, W. M., and Zachariasen, F. (**1976b**). "Sound propagation through a fluctuating stratified ocean: Theory and observation," J. Acoust. Soc. Am. **59**, 818–838.

Pederson, M. A. (**1961**). "Acoustic intensity anomalies introduced by constant velocity gradients," J. Acoust. Soc. Am. **33**, 465–474.

Pederson, M. A., and Gordon, D. F. (**1967**). "Comparison of curvilinear and linear profile approximation in the calculation of underwater sound intensities by ray theory," J. Acoust. Soc. Am. **41**, 419–438.

Pinkel, R. (**1984**). "Doppler sonar observations of internal waves: The wavenumber-frequency spectrum," J. Phys. Oceanogr. **14**, 1249–1270.

Press, W. H., Flannery, B. P., Teukolsky, S. A., and Vetterling, W. T. (**1986**). *Numerical Recipes* (Cambridge U.P., Cambridge).

Smith, K. B., Brown, M. G., and Tappert, F. D. (**1992a**). "Ray chaos in underwater acoustics," J. Acoust. Soc. Am. **91**, 1939–1949.

Smith, K. B., Brown, M. G., and Tappert, F. D. (**1992b**). "Acoustic ray chaos induced by mesoscale ocean structure," J. Acoust. Soc. Am. **91**, 1950–1959.

Weinberg, H. (**1975**). "Application of ray theory to acoustic propagation in horizontally stratified oceans," J. Acoust. Soc. Am. **58**, 97–109.

Woods, M. T., and Okal, E. A. (**1987**). "Effect of variable bathymetry on the amplitude of teleseismic tsunamis: A ray-tracing experiment," Geophys. Res. Lett. **14**, 765–768.

Worcester, P. F., Cornuelle, B. D., Hildebrand, J. A., Hodgkiss, W. S., Jr., Duda, T. F., Boyd, J., Howe, B. M., Mercer, J. M., and Spindel, R. C., "A comparison of measured and predicted broadband acoustic arrival patterns in travel-time depth coordinates at 1000-km range," J. Acoust. Soc. Am. **95**, 3118–3128 (1994).